Measurement of the unresolved $^9Be^+$ $^2P_{3/2}$ hyperfine splittings using quantum-interference-enhanced state-selective repump spectroscopy

D. M. Fairbank,* A. L. Banducci, R. W. Gunkelman,† J. B. VanArsdale, and S. M. Brewer‡
Department of Physics, Colorado State University, Fort Collins, Colorado 80523, USA

(Received 3 November 2023; accepted 13 December 2023; published 16 January 2024)

Hyperfine splittings of the $^2P_{3/2}$ manifold in $^9Be^+$ were measured directly using a single laser-cooled ion stored in a radiofrequency Paul trap. As the hyperfine structure is unresolved beneath the natural linewidth of the transition, manipulation of the initial state, polarization, and final-state populations was used to preferentially detect scattering events through specific intermediate excited states. While quantum interference effects typically complicate the modeling of unresolved measurement lineshapes, in this work quantum interference helped to suppress extraneous scattering components. The hyperfine splittings between the $|^2P_{3/2}, F = 3\rangle$ state and the $|^2P_{3/2}, F = 2\rangle$ and $|^2P_{3/2}, F = 1\rangle$ states were measured to be $\Delta\nu_{32} = 0.801(56)$ MHz and $\Delta\nu_{31} = 5.050(83)$ MHz, respectively.

DOI: 10.1103/PhysRevA.109.012809

I. INTRODUCTION

Measurements of the fine and hyperfine structure in simple atomic systems can be used for stringent tests of many-body quantum electrodynamics calculations [1–3] or be used in combination with theory to extract subtle information about the nucleus, such as the relative charge radii between isotopes or the nuclear Zemach radius [4–7]. The electromagnetic multipole moments of the nucleus can also be extracted from measured hyperfine structure. While the nuclear magnetic dipole moment can be determined from the ground-state hyperfine splitting in alkali-like systems, determination of higher-order contributions requires probing higher angular momentum states [8]. For example, $^2P_{3/2}$ hyperfine structure measurements have been used previously to extract nuclear magnetic octupole moments in both ^{133}Cs [9,10] and ^{87}Rb [11]. Interest in understanding such nuclear structure of light atoms has persisted over many decades, including recent theory and proposal to extend measurements to muonic Li^{2+}, Be^{3+} and B^{4+} [12].

$^9Be^+$ has been the focus of study in prior theoretical works [2,13] and has been widely used in ion-trap and ion-beam experiments dating back several decades. It is a particularly convenient ion to Doppler cool, requiring only a single 313-nm laser tuned to the D_2 closed cycling transition. It also has a long-lived ground-state hyperfine qubit due to its nuclear spin of $\frac{3}{2}$. Thus, $^9Be^+$ has served as an ion for sympathetic cooling and state readout in quantum logic clocks [14,15], as a qubit for quantum information processing [16,17], and as a platform for precision measurement of a simple three-electron atomic system [18]. While the $^2S_{1/2}$ and $^2P_{1/2}$ hyperfine splittings in $^9Be^+$ have previously been measured [4,18–20], the $^2P_{3/2}$ hyperfine splitting of a few MHz has remained difficult to observe directly, unresolved beneath the $\approx$ 20-MHz natural linewidth.

A wide variety of methods have been developed for measurement of both resolved and unresolved hyperfine structures of alkali atoms [21], but for the $^2P_{3/2}$ structure of alkali-like $^9Be^+$, only rough bounds have been set experimentally using zero-field quantum beat spectroscopy [22]. The method applied here utilizes quantum interference and state-selective repump spectroscopy techniques to enable direct optical measurements with high specificity to individual $|^2P_{3/2}, F, m_F\rangle$ states at low magnetic field. The spectroscopy is performed on a single trapped ion, applying a framework developed for spectroscopy of strong transitions that accounts for photon recoil in an intermediate confinement regime [18]. Using a single ion also simplifies high-fidelity initialization into a single $|^2S_{1/2}, F, m_F\rangle$ ground state and the exchange and preferential detection of final-state populations throughout the $^2S_{1/2}$ manifold. With this approach, we have measured the frequency difference between three separate D_2 transitions to determine the hyperfine splittings between $|^2P_{3/2}, F = 3\rangle$ and $|^2P_{3/2}, F = 2\rangle$ ($\Delta\nu_{32}$) and between $|^2P_{3/2}, F = 3\rangle$ and $|^2P_{3/2}, F = 1\rangle$ ($\Delta\nu_{31}$). The measurement configurations are summarized in Fig. 1.

II. EXPERIMENT

The ion trap and laser systems used in this work have been described in detail previously [18]. The linear radiofrequency (rf) Paul trap is a revised version of the wheel trap used in the aluminum-ion quantum logic clock [23,24], with gold electrodes on a diamond wafer and separate titanium endcaps spaced 4 mm from the center of the trap. A frequency stabilized ultraviolet laser at $\lambda = 313$ nm is used for Doppler cooling, optical pumping, and state readout. The ion trap operates with an rf drive frequency of $\Omega_{rf}/2\pi = 78.93$ MHz and a differential drive amplitude of approximately ± 168 V. The secular mode frequencies of a single $^9Be^+$ ion are $\omega_z/2\pi \approx 3.65$ MHz for the axial mode

*d.fairbank@colostate.edu
†Current address: Stable Laser Systems, Boulder, CO 80301.
‡samuel.brewer@colostate.edu

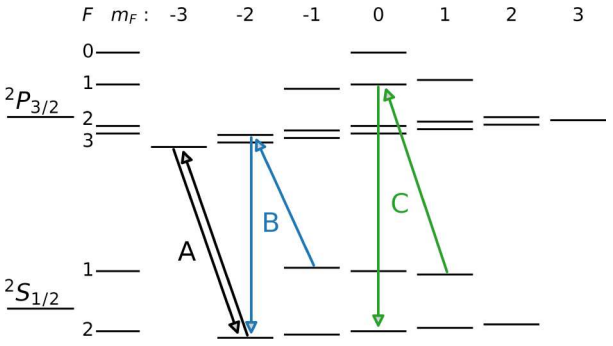

FIG. 1. Energy level diagram for the $^2S_{1/2}$ and $^2P_{3/2}$ states in $^9Be^+$. The measurement configurations used to observe the hyperfine splittings are labeled as A, B, and C. "A" is the σ^- cycling transition, also used for Doppler cooling and state detection. "B" is a standard repump configuration which scatters only through $|^2P_{3/2}, 2, -2\rangle$. "C" is a configuration which preferentially detects scatter through $|^2P_{3/2}, 1, 0\rangle$ to $|^2S_{1/2}, 2, 0\rangle$. Splittings are recorded as difference frequencies, $\Delta\nu_{32} = \nu_B - \nu_A$ and $\Delta\nu_{31} = \nu_C - \nu_A$, after correction for the magnetic field contributions and $^2S_{1/2}$ hyperfine structure. Note that the 1–5-MHz $^2P_{3/2}$ hyperfine splittings are shown exaggerated in scale relative to the 1.25-GHz $^2S_{1/2}$ splitting

and $\omega_x/2\pi \approx 9.8$ MHz and $\omega_y/2\pi \approx 10.6$ MHz for the radial modes. A quantization axis magnetic field of $B = 13.43$ μT is used to produce ≈ 100-kHz separation between Zeeman sublevels. This low field value allows sufficient frequency separation between the states, while avoiding level crossings in the $^2P_{3/2}$ manifold that occur at higher field. The bias field is determined from measurements of the $|^2S_{1/2}, 2, -2\rangle \leftrightarrow |^2S_{1/2}, 1, -1\rangle$ transition ($\nu_{-2,-1} \approx 1250.3$ MHz). Stray magnetic fields on orthogonal axes are canceled using additional sets of magnetic field coils. A 50-mm-diameter rf loop antenna is positioned just above the fluorescence collection window, outside the vacuum chamber above the trap. This is used to drive all microwave transitions between $|^2S_{1/2}, F, m_F\rangle$ states. The frequencies and pulses are generated by an externally referenced direct digital synthesizer. The fundamental rf frequencies are quadrupled to reach the required range of $\nu \approx 1250$ MHz. The microwave signal is amplified and then filtered to suppress other harmonic components.

All optical frequencies for this experiment are generated from a single laser. The laser frequency is stabilized to a wavemeter at a frequency that is detuned by ≈ −650 MHz from the $|^2S_{1/2}, 2, -2\rangle \rightarrow |^2P_{3/2}, 3, -3\rangle$ closed cycling transition. The laser frequencies are then adjusted using acousto-optic modulators (AOMs). The resonant detection beam is shifted up in frequency by ≈ 650 MHz and the repump beams are shifted down by ≈ 600 MHz to span the full 1.25-GHz ground-state splitting. A cat-eye configuration is used for the double-pass AOM beams to suppress beam pointing variation [24]. The spatial profile is cleaned with a pinhole spatial filter and then power stabilized via feedback on the AOM drive power.

The excited-state hyperfine splitting is determined as the sum of the AOM shifts for the cycling and repump transitions, minus the ground-state contribution for each configuration. As absolute frequency measurements are not necessary, we determine only the relative splittings, $\Delta\nu_{32} = B - A$ and $\Delta\nu_{31} = C - A$ (see Fig. 1), after correction for the magnetic field and $^2S_{1/2}$ hyperfine contributions. The frequency of the line center in A is determined by measurement before and after each repump measurement (B or C) with a linear interpolation using the time stamps of the scans. This is done to eliminate the effect of slow linear drift in the absolute frequency of the wavemeter lock point. The wavemeter tends to drift approximately 3 MHz over a single day, while a single set of measurements takes roughly 30 minutes. Drifts beyond the linear model are small, and negligible at the current measurement uncertainty.

At the start of each measurement, the ion is cooled using 1 ms of far-detuned ($\Delta/2\pi = -415$ MHz) laser cooling and 500 μs of near-detuned Doppler cooling ($\Delta/2\pi = -10$ MHz) on the $|^2S_{1/2}, 2, -2\rangle \rightarrow |^2P_{3/2}, 3, -3\rangle$ cycling transition ($\Gamma/2\pi \approx 19.64$ MHz [25]). The measured temperature after cooling is consistent with the Doppler cooling limit of ≈ 0.5 mK. The cooling sequence also optically pumps the population into $|^2S_{1/2}, 2, -2\rangle$ with a measured purity ⩾ 98.6%. For repump measurements, the population is then coherently transferred to either of the other initial $|^2S_{1/2}, F, m_F\rangle$ states using a sequence of microwave pulses.

After the population is initiated into the desired state, an optical spectroscopy pulse is applied to the ion. In all cases the intensity on the ion corresponds to a saturation parameter of $S_0 \leqslant 0.02$. Each point is the average of 200 individual measurements. A single lineshape is generated from a further four to six averages of 200 points over a scan range of about ±60 MHz, with the order of measurement points randomized for each cycle. For measurements on the σ^- closed cycling transition (Fig. 1, A), a 250-μs pulse is applied and photons are counted as the frequency is adjusted in steps across the transition. For repump measurements (Fig. 1, B and C), the pulse duration is set between ≈ 5–50 μs and adjusted to limit repump saturation broadening.

While measurements A and B scatter only through a single excited state, it is necessary to account for several nonzero scattering amplitudes in measurement C. This is done using the quantum interference formalism presented in Ref. [5], that was simplified for repump style measurements starting from a single ground state in Ref. [18]. As a brief summary, the scattering rate from initial ground state $|i\rangle$ to final ground state $|f\rangle$, with scatter through intermediate excited states $|F', m'\rangle$, is calculated according to

$$R_{i\to f} = \frac{I}{I_0}\left(\frac{\Gamma}{2}\right)^3 \left| \sum_{F'} \frac{\left(A^{F'm'}_{F_f m_f}\right)_{q_s}\left(A^{F'm'}_{F_i m_i}\right)_{q_L}}{\Delta^{F'}_{F_i} + i\Gamma/2} \right|^2, \qquad (1)$$

with a sum of amplitudes within the square capturing the interference between the components. I_0 is a defined reference intensity, Γ is the natural linewidth of the transition and $\Delta^{F'}_{F_i}$ is the laser detuning. The expression here is already simplified for the case of a single initial state, laser polarization q_L and scattering polarization q_s. The numerator contains the relative scattering amplitude of a given component, proportional to the product of excitation and decay matrix elements. Interference between states is most prominent for unresolved structure, where the relative detuning between the components is small compared to the natural linewidth. More details are given in Refs. [5,18].

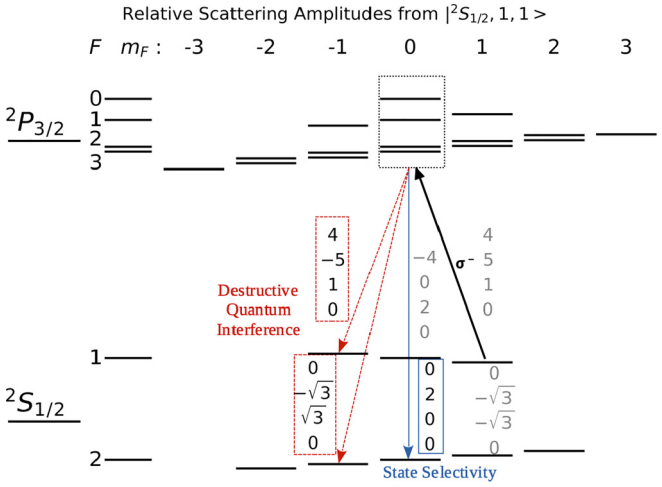

FIG. 2. Relative scattering amplitudes for measurement C, with σ^- polarization and population starting in $|^2S_{1/2}, 1, 1\rangle$. The four numbers listed (top to bottom) for each final state represent amplitudes associated with scatter through $^2P_{3/2}$ excited states $F = 0$, 1, 2, 3, $m_F = 0$, respectively. The values are products of the excitation matrix element from initial state $|^2S_{1/2}, 1, 1\rangle$ and the decay matrix element to each given final state. Population starting in $|^2S_{1/2}, 1, 1\rangle$ can scatter to $|^2S_{1/2}, 2, 0\rangle$ only through $|^2P_{3/2}, 1, 0\rangle$ (all other amplitudes are zero). Population scattering to $|^2S_{1/2}, 1, -1\rangle$ and $|^2S_{1/2}, 2, -1\rangle$ is largely suppressed by quantum interference (the sum of the amplitudes is zero), outside of the effects of the small relative detuning differences between hyperfine components. This helps to improve the contrast of the signal. After the spectroscopy pulse, final-state populations are exchanged using microwave pulses to preferentially detect the generated $|^2S_{1/2}, 2, 0\rangle$ component.

The relative scattering amplitudes for measurement C are given in Fig. 2. Scatter from $|^2P_{3/2}, 1, 0\rangle$ is measured by preferential detection of the generated $|^2S_{1/2}, 2, 0\rangle$ population. Quantum interference is helpful in suppressing scatter to both $|^2S_{1/2}, 2, -1\rangle$ and $|^2S_{1/2}, 1, -1\rangle$, which improves measurement specificity and contrast.

The final step of each repump measurement sequence is resonant state detection. The unequal brightness of $|^2S_{1/2}, F, m_F\rangle$ states is used to preferentially detect individual components. Any population in the $|^2S_{1/2}, 2, -2\rangle$ state produces the most counts, followed by populations in $|^2S_{1/2}, 2, -1\rangle$ and $|^2S_{1/2}, 2, 0\rangle$. If a state population other than $|2, -2\rangle$ needs to be measured, a series of microwave pulses is used to move that population to $|2, -2\rangle$ and put other major population components into darker states. In the particular case of measurement C, microwave pulses are applied which rearrange the final $|F, m_F\rangle$ state populations $|2, -2\rangle \rightarrow |2, -1\rangle$, $|2, -1\rangle \rightarrow |2, 0\rangle$, and $|2, 0\rangle \rightarrow |2, -2\rangle$ to enhance the $|2, 0\rangle$ component.

The number of counts detected from each final state during a readout pulse is calibrated experimentally. In this case the typical relative brightness of the $F = 2$ ground states from $m_F = -2$ to $m_F = +2$ are approximately 1, 0.38, 0.18, 0.06, and 0.05, respectively. This trend can also be predicted from the relative probabilities of decays to $F = 1$ dark states using the quantum interference model. All of the $|^2S_{1/2}, F = 1\rangle$ states are relatively dark due to the ≈ 1.25-GHz

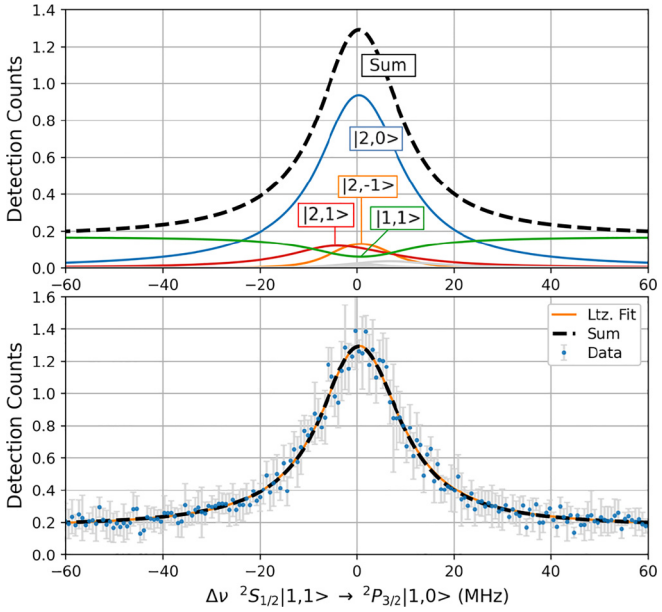

FIG. 3. (Top) Calculated spectral contributions for measurement C in the case of a moderate-duration spectroscopy pulse. The major contributions from individual final-state populations are labeled. Population ending in $|^2S_{1/2}, 2, 0\rangle$ comes primarily from scatter from $|^2S_{1/2}, 1, 1\rangle$ through $|^2P_{3/2}, 1, 0\rangle$ and is detected preferentially by moving the $|2, 0\rangle$ population to the brightest state, $|2, -2\rangle$. Other major populations generated are exchanged to darker states to reduce their contributions to the lineshape. The total lineshape, when fit with a single component Lorentzian, appears shifted higher in frequency by approximately 200 kHz, with some pulse-duration dependence. This originates from imperfect isolation of the final $|^2S_{1/2}, 2, 0\rangle$ population and from secondary scatter during the spectroscopy pulse as some population also starts to accumulate in $|^2S_{1/2}, 1, 0\rangle$. (Bottom) A single data set is shown for measurement C, with statistical error bars on individual points. The data set is fit with a Lorentzian lineshape (orange). The total calculated lineshape from the top section (black dashed) is superimposed over the data.

detuning, but do still generate some small residual counts of approximately 0.05, 0.04 and 0.03, respectively, for $m_F = -1$ to $m_F = +1$.

The full lineshape model is generated by first calculating the relative scattering amplitudes and rates of population transfer using the quantum interference formalism [5,18], solving the differential equations as an initial value problem to determine the expected final $^2S_{1/2}$ population distribution, and then scaling the populations by the calibrated brightness of each state during resonant D_2 detection. A simulated lineshape for measurement C applying this methodology is shown in Fig. 3.

III. CHARACTERIZATION OF SHIFTS AND UNCERTAINTIES

A summary of measurement uncertainties is shown in Table I. The dominant common systematic uncertainty is a slight residual slope in the power stabilization of the laser across the frequency range spanned by each double-pass AOM. The stabilization is within 3% across the full scan

TABLE I. Statistical and systematic uncertainties in kHz for the $^2P_{3/2}$ hyperfine splittings, $\Delta\nu_{32}$ and $\Delta\nu_{31}$.

Effect	$\Delta\nu_{32}$	$\Delta\nu_{31}$
Statistical variation	35	49
Optical power stabilization	36	36
Photon recoil effects	25	25
Scattering line-shape model	0	50
Magnetic field drift	<2	<2
AC Stark shift (optical)	<1	<1
Imperfect laser polarization	<1	<1
Total	56	83

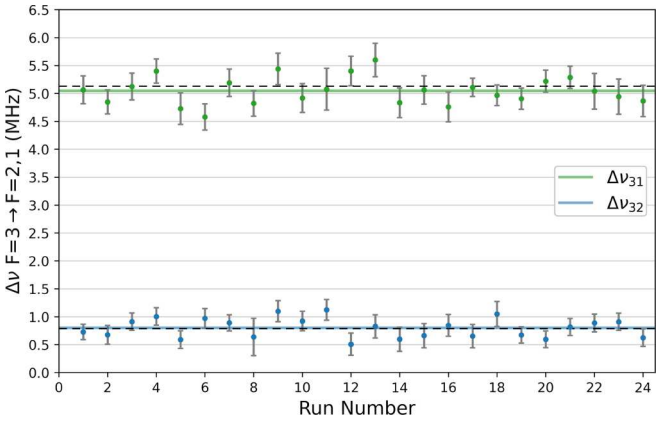

FIG. 4. Consecutive measurements are shown for $\Delta\nu_{31}$ (top) and $\Delta\nu_{32}$ (bottom). The minor Zeeman contributions to the ground and excited states have been removed to give the zero-field values. Splittings calculated from the effective hyperfine constants from theory are shown as dashed lines, with uncertainty-weighted fits to the experimental data shown as solid lines. Error bars represent the statistical uncertainty for each individual measurement set. The reduced χ^2 values for $\Delta\nu_{31}$ and $\Delta\nu_{32}$ measurements are 1.00 and 0.97, respectively. Note that the upper and lower data are not correlated since $\Delta\nu_{31}$ and $\Delta\nu_{32}$ measurements were taken on different days.

range, which contributes up to 25-kHz uncertainty in determination of the line center. Because the beams for the cycling transition and repump are shifted through independent AOMs, with feedback parameters determined independently, we apply this uncertainty contribution from each beam in quadrature.

Photon recoil affects both the cycling transition and the repump measurements, with a correction applied individually to each. These effects have been characterized previously [18], and both the effective photon recoil shift and heating are accounted for here. The recoil and heating corrections mostly cancel when measuring a frequency difference between cycling and repump measurements, with a residual relative correction of 25 kHz. This correction is attributable to the mild difference in heating during a closed cycling transition measurement versus a repump measurement which scatters fewer photons. The uncertainty in the correction is ± 25 kHz, related to calibration of the heating and number of scattering events.

The observed lineshape in the $\Delta\nu_{31}$ measurement depends mildly on the repump pulse duration and intensity. A correction is applied individually to each measurement depending on the experimental conditions and ranges from -100 to -300 kHz. Calibration of the experimental conditions used in the model contributes an uncertainty of 50 kHz in the extracted transition frequency, which is applied as a common systematic in the $\Delta\nu_{31}$ results.

Polarization impurity contributes only a negligible systematic uncertainty in these measurements. The σ^- polarization, which all spectroscopy beams share, can be tuned with such precision (by iteratively adjusting a combination of polarizer, waveplates with both axial rotation and tip/tilt, beam pointing and magnetic field, while observing histograms of the cycling transition counts) that σ^+ and π impurity components are negligible [18].

To extract the final frequency splittings, we apply corrections for the ground-state hyperfine splittings and the ground- and excited-state Zeeman shifts due to applied bias magnetic field. Ground-state contributions are calculated with the generalized Breit-Rabi formula, using the experimentally determined value $A_{S_{1/2}} = -625\,008\,837.044(12)$ Hz [20]. The Zeeman corrections for the excited states are first approximated assuming a linear shift. We then take the best-fit hyperfine coefficients and iteratively determine the full magnetic field shift, including the hyperfine-associated curvature, using the eigenvalues of the combined $^2P_{3/2}$ hyperfine and Zeeman Hamiltonian.

The theoretical excited-state hyperfine constants used for comparison in this work are $A_{P_{3/2}} = -1.023(3)$ MHz, and $B_{P_{3/2}} = 2.290(6)$ MHz [2,13,26]. The value for the $B_{P_{3/2}}$ coefficient is corrected to account for a previous sign error in the literature and is scaled using the latest extracted value for the ^{9}Be nuclear electric quadrupole moment [26,27]. It should be noted that the hyperfine coefficients given are effective values, already adjusted to account for second-order hyperfine-induced fine structure mixing of the ^2P manifold and various other corrections [2]. The ^{9}Be nuclear magnetic octupole moment has not yet been measured, but was approximated at $\Omega = -0.073$ $(b \times \mu_N)$ [28]. A corresponding first-order $C_{P_{3/2}}$ coefficient has not been reported. We have calculated the second-order hyperfine-induced fine structure mixing contribution. By combining any two of the three reported fine structure mixing corrections from Ref. [2], $\delta A_{P_{1/2}} = -6.83$ kHz, $\delta A_{P_{3/2}} = -2.76$ kHz, and $\delta B_{P_{3/2}} = -18.03$ kHz, with the equations for the $I = \frac{3}{2}$ case in Ref. [29], it is possible to determine the second-order coefficients $\eta = -516.4$ kHz and $\zeta = -36.5$ kHz. The coefficients lead to a correction term $\delta C_{P_{3/2}} = -0.041$ kHz. This contribution is negligible at the present measurement uncertainty.

IV. RESULTS AND DISCUSSION

Individual measurement results are shown in Fig. 4, with final uncertainty weighted results in Table II. The measurements of $\Delta\nu_{32}$ and $\Delta\nu_{31}$ agree with the calculated values [2], within the experimental uncertainty. Further experimental precision could enable a more stringent test or help determine the effective $C_{P_{3/2}}$ coefficient and extract the magnetic octupole moment. It should be possible to improve the power stability

TABLE II. Measured $^2P_{3/2}$ hyperfine splittings, $\Delta\nu_{32}$ and $\Delta\nu_{31}$, in comparison to calculated values. The effective hyperfine constants, $A_{P_{3/2}}$ and $B_{P_{3/2}}$, from theory are listed. The extracted hyperfine constants are a best fit to the two measured splittings. All values are in units of MHz.

$\Delta\nu_{32}$	$\Delta\nu_{31}$	$A_{P_{3/2}}$	$B_{P_{3/2}}$	Ref.
0.788	5.130	−1.023(3)	2.290(6)	Theory[a]
0.801(56)	5.050(83)	−1.01(2)	2.23(8)	This work

[a]Puchalski and Pachucki (2009) [2].

of the spectroscopy laser by using a faster feedback method. To reduce the uncertainty due to photon recoil heating, it would be possible to add a sympathetic cooling ion, use lower exposure spectroscopy pulses, or apply stronger trap confinement. To reach the few-kHz level of uncertainty with this method would require splitting the 20-MHz linewidth by about 1 part in 4000.

In conclusion, we have presented direct optical measurements of two unresolved hyperfine splittings of the $^2P_{3/2}$ manifold in $^9Be^+$. The measurements to $|^2P_{3/2}, F = 1\rangle$ demonstrate a particular adaptation of repump spectroscopy utilizing quantum interference and selection rules to distinguish otherwise unresolved structure. The final results for the splittings are in good agreement with calculation using hyperfine constants from theory, within the experimental uncertainty.

ACKNOWLEDGMENTS

We thank C. Sanner and D. Yost for useful discussions and careful reading of the manuscript. We thank K. Pachucki, M. Puchalski, and V. Yerokhin for helpful communications and guidance regarding the $B_{P_{3/2}}$ hyperfine constant used for this work. This work was supported by Colorado State University, National Science Foundation Grant No. PHY-2110102, Office of Naval Research Grant No. N00014-22-1-2070, and NIST Precision Measurement Grant No. 70NANB22H218.

[1] Z.-C. Yan and G. W. F. Drake, Phys. Rev. A **61**, 022504 (2000).
[2] M. Puchalski and K. Pachucki, Phys. Rev. A **79**, 032510 (2009).
[3] M. Puchalski and K. Pachucki, Phys. Rev. A **92**, 012513 (2015).
[4] W. Nörtershäuser, D. Tiedemann, M. Žáková, Z. Andjelkovic, K. Blaum, M. L. Bissell, R. Cazan, G. W. F. Drake, C. Geppert, M. Kowalska, J. Krämer, A. Krieger, R. Neugart, R. Sánchez, F. Schmidt-Kaler, Z.-C. Yan, D. T. Yordanov, and C. Zimmermann, Phys. Rev. Lett. **102**, 062503 (2009).
[5] R. C. Brown, S. Wu, J. V. Porto, C. J. Sansonetti, C. E. Simien, S. M. Brewer, J. N. Tan, and J. D. Gillaspy, Phys. Rev. A **87**, 032504 (2013).
[6] A. Antognini, F. Hagelstein, and V. Pascalutsa, Annu. Rev. Nucl. Part. Sci. **72**, 389 (2022).
[7] M. Puchalski and K. Pachucki, Phys. Rev. Lett. **111**, 243001 (2013).
[8] E. Arimondo, M. Inguscio, and P. Violino, Rev. Mod. Phys. **49**, 31 (1977).
[9] V. Gerginov, A. Derevianko, and C. E. Tanner, Phys. Rev. Lett. **91**, 072501 (2003).
[10] D. Das and V. Natarajan, J. Phys. B: At., Mol. Opt. Phys. **41**, 035001 (2008).
[11] V. Gerginov, C. E. Tanner, and W. Johnson, Can. J. Phys. **87**, 101 (2009).
[12] A. E. Dorokhov, A. A. Krutov, A. P. Martynenko, F. A. Martynenko, and O. S. Sukhorukova, Phys. Rev. A **98**, 042501 (2018).
[13] V. A. Yerokhin, Phys. Rev. A **78**, 012513 (2008).
[14] T. Rosenband *et al.*, Science **319**, 1808 (2008).
[15] S. A. King, L. J. Spieß, P. Micke, A. Wilzewski, T. Leopold, E. Benkler, R. Lange, N. Huntemann, A. Surzhykov, V. A. Yerokhin, J. R. Crespo López-Urrutia, and P. O. Schmidt, Nature (London) **611**, 43 (2022).
[16] D. J. Wineland, C. Monroe, W. M. Itano, D. Leibfried, B. E. King, and D. M. Meekhof, J. Res. Natl. Inst. Stand. Technol. **103**, 259 (1998).
[17] J. P. Gaebler, T. R. Tan, Y. Lin, Y. Wan, R. Bowler, A. C. Keith, S. Glancy, K. Coakley, E. Knill, D. Leibfried, and D. J. Wineland, Phys. Rev. Lett. **117**, 060505 (2016).
[18] D. M. Fairbank, A. L. Banducci, R. W. Gunkelman, J. B. VanArsdale, M. L. Vildibill, and S. M. Brewer, Phys. Rev. Lett. **131**, 093001 (2023).
[19] J. J. Bollinger, J. S. Wells, D. J. Wineland, and W. M. Itano, Phys. Rev. A **31**, 2711 (1985).
[20] N. Shiga, W. M. Itano, and J. J. Bollinger, Phys. Rev. A **84**, 012510 (2011).
[21] M. Allegrini, E. Arimondo, and L. A. Orozco, J. Phys. Chem. Ref. Data **51**, 043102 (2022).
[22] O. Poulsen, T. Andersen, and N. J. Skouboe, J. Phys. B **8**, 1393 (1975).
[23] S. M. Brewer, J.-S. Chen, A. M. Hankin, E. R. Clements, C. W. Chou, D. J. Wineland, D. B. Hume, and D. R. Leibrandt, Phys. Rev. Lett. **123**, 033201 (2019).
[24] J.-S. Chen, Ph.D. thesis, University of Colorado, Boulder, 2017.
[25] T. Andersen, K. A. Jessen, and G. Sørensen, Phys. Rev. **188**, 76 (1969).
[26] K. Pachucki, M. Puchalski, and V. A. Yerokhin (private communication).
[27] M. Puchalski, J. Komasa, and K. Pachucki, Phys. Rev. Res. **3**, 013293 (2021).
[28] K. Beloy, A. Derevianko, and W. R. Johnson, Phys. Rev. A **77**, 012512 (2008).
[29] K. Beloy and A. Derevianko, Phys. Rev. A **78**, 032519 (2008).